3-2009

Simulated Scatter Performance of an Inverse-Geometry Dedicated Breast CT System

Reema Bhagtani
Marquette University

Taly Gilat Schmidt
Marquette University, tal.gilat-schmidt@marquette.edu

Medical Physics, Vol. 36, No. 3 (March 2009): 788-796. DOI.

Simulated Scatter Performance of An Inverse-Geometry Dedicated Breast CT System

Reema Bhagtani
Department of Biomedical Engineering, Marquette University, Milwaukee, Wisconsin
Taly Gilat Schmidt
Department of Biomedical Engineering, Marquette University, Milwaukee, Wisconsin

Abstract

The purpose of this work was to quantify the effects of scatter for inverse-geometry dedicated breast CT compared to cone-beam breast CT through simulations. The inverse geometry was previously proposed as an alternative to cone-beam acquisition for volumetric CT. The inverse geometry consists of a large-area scanned-source opposite a detector array that is smaller in the transverse direction. While the gantry rotates, the x-ray beam is rapidly sequenced through an array of positions, acquiring a truncated projection image at each position. Inverse-geometry CT (IGCT) is expected to detect less scatter than cone-beam methods because only a fraction of the object is irradiated at any time and the fast detector isolates the measurements from sequential x-ray beams. An additional scatter benefit is the increased air gap due to the inverted geometry. In this study,

we modeled inverse-geometry and cone-beam dedicated breast CT systems of equivalent resolution, field of view, and photon fluence. Monte Carlo simulations generated scatter and primary projections of three cylindrical phantoms of diameters 10, 14, and 18 cm composed of 50% adipose/50% glandular tissue. The scatter-to-primary ratio (SPR) was calculated for each breast diameter. Monte Carlo simulations were combined with analytical simulations to generate inverse-geometry and cone-beam images of breast phantoms embedded with tumors. Noise representing the photon fluence of a realistic breast CT scan was added to the simulated projections. Cone-beam data were reconstructed with and without an ideal scatter correction. The CNR between breast tumor and background was compared for the inverse and cone-beam geometries for the three phantom diameters. Results demonstrated an order of magnitude reduction in SPR for the IGCT system compared to the cone-beam system. For example, the peak IGCT SPRs were 0.05 and 0.09 for the 14 and 18 cm phantoms, respectively, compared to 0.42 and 1 for the cone-beam system. For both geometries, the effects of scatter on contrast-to-noise ratio (CNR) were small for the 10 cm diameter phantom. The inverse-geometry improved the CNR by factors of 1.16 for the 14 cm phantom and 1.48 for the 18 cm phantom compared to a cone-beam acquisition without scatter correction. When an ideal scatter correction was applied to the cone-beam acquisition, the IGCT CNR improvements were 1.03 and 1.25 for the 14 and 18 cm phantoms. Overall, the results suggest that the inverse geometry may be advantageous for dedicated breast CT, an application that requires high-contrast resolution, spatial resolution, and dose efficiency.

I. INTRODUCTION

Dedicated breast computed tomography (CT) is a promising technology for acquiring volumetric images of the breast with isotropic, submillimeter resolution at dose levels equivalent to mammography and without breast compression.[1,2] Numerous studies have investigated the performance of breast CT with respect to image quality and radiation dose.[3–15] In an initial clinical trial, breast CT was more effective for depicting masses and less effective for depicting calcifications compared to mammography.[16]

In dedicated breast CT, the patient lies prone with the breast to be imaged positioned through an opening in the table. The CT gantry, composed of a source and detector, is located beneath the table and rotates about the breast. The majority of proposed breast CT systems utilize an x-ray tube which emits a half-cone-beam towards a flat-panel detector, as illustrated in Fig. **1**. While the cone-beam geometry enables rapid acquisition of the breast volume, it also leads to several image quality limitations.

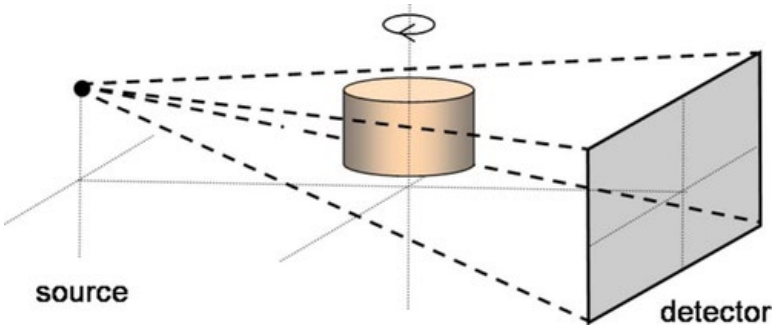

Figure 1 Cone-beam dedicated breast CT geometry consisting of an x-ray source and a large-area detector.

One limitation is that an axially scanned cone-beam acquisition does not sufficiently sample the volume, which may cause artifacts as the cone angle increases.[17] Alternative breast CT scanning trajectories have been proposed to provide sufficient volumetric sampling.[18–20] Because cone-beam systems instantaneously irradiate a large volume, scattered radiation is an additional image quality concern. Scattered radiation decreases the contrast and contrast-to-noise ratio (CNR) in CT images and also introduces artifacts.[21–24] Numerous techniques have been proposed to mitigate the effects of scatter for cone-beam CT. One approach is to reduce the

scattered radiation that reaches the detector, for example by using slot collimators, grids, or an air gap.[25,27] Another approach is to correct for the effects of scattered radiation after acquisition by either measuring or modeling the scatter signal.[28–34] While these postacquisition correction methods may reduce the deterministic effects of scatter, i.e., the cupping artifacts and contrast loss, they cannot correct for the stochastic contribution of scattered radiation.

Several studies have investigated the magnitude and reduction in scatter specifically for dedicated breast CT. The scatter-to-primary ratio (SPR) of a dedicated breast CT system was experimentally measured to range from 0.2 to 1 depending on breast size and composition.[7] In this study, the use of grids and air gaps provided a limited reduction in SPR. A multislit multislice system (MSMS) has been proposed to enable low-scatter acquisition with a photon-counting detector.[26] The mechanical scanning of the slot collimators in the MSMS may necessitate longer scan times. In the proposed MSMS configuration, the source is stationary, resulting in cone-beam sampling. A postacquisition scatter correction algorithm has been proposed for breast CT that reduces the cupping artifacts but does not recover the loss in contrast.[34]

Breast imaging is a challenging task that requires high-contrast resolution to depict masses, high spatial resolution to depict calcifications, and low dose, especially for screening applications. Therefore it is important to reduce the effects of scatter in order to improve the contrast performance and dose efficiency of breast CT systems. The inverse geometry is an alternative volumetric CT technique with the potential for scatter reduction.[35] Inverse-geometry CT (IGCT), illustrated in Fig. **2**, consists of a large-area scanned source opposite a detector array that is smaller than the source in the transverse direction. The implementation and performance of a prototype table-top IGCT system was described previously.[36] The prototype system utilized a scanned transmission-anode x-ray source and a photon-counting detector (NovaRay Inc., Newark, CA).[37,38] While the gantry rotates, the electron beam is rapidly and electromechanically steered behind the transmission target. The beam dwells for $1\ \mu s$ at each of an array of positions, where the resulting x-ray beam is collimated to illuminate the detector. At each source position, a truncated projection of the object is acquired. Because the IGCT source and detector have the same longitudinal extent, sufficient volumetric sampling is achieved. The detected scatter is reduced compared to a conventional cone-beam system because only a fraction of the object is irradiated at any time while the fast detector isolates the measurements from sequential beams. An additional scatter benefit is the increased air gap that occurs when the conventional geometry is inverted. Previous IGCT investigations demonstrated the feasibility of subsecond scan times for a $15\ \mathrm{cm}$ thick volume, $0.25\ \mathrm{mm}$ isotropic resolution, and negligible cone-beam artifacts.[35,36] To our knowledge, the scatter performance of IGCT has not been quantified for any application.

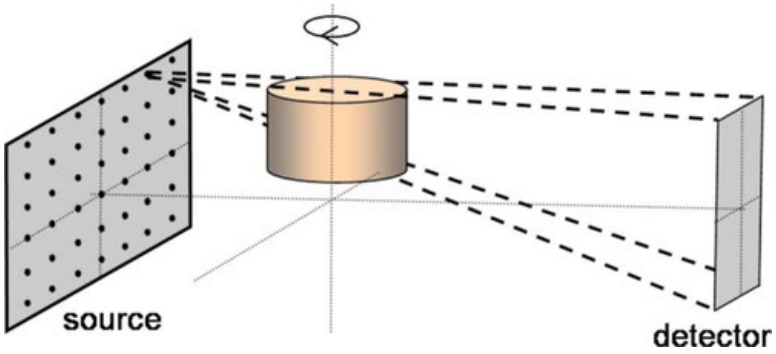

Figure 2 Inverse-geometry dedicated breast CT consisting of a large-area scanned source and a narrower detector array.

The inverse geometry, which has the potential for increased dose efficiency due to scatter reduction and photon-counting detection, may be advantageous for dedicated breast CT scanning. In this study, we

investigated the scatter performance of the inverse geometry compared to the cone-beam geometry for dedicated breast CT. We quantified the SPR of comparable inverse-geometry and cone-beam systems for a range of breast diameters through simulations. We also investigated the effects of scatter on the CNR of both inverse and cone-beam geometries.

II. MATERIALS AND METHODS

II.A. Monte Carlo simulations

Our goal was to quantify the magnitude and impact of detected scatter for a breast IGCT system and a comparable cone-beam breast CT system. In order to isolate the effects of scatter, the IGCT and cone-beam systems were simulated with equivalent field of view (FOV), spatial resolution, detectors, photon fluence, and spectrum. Table **I** lists the specifications of the simulated cone-beam and inverse-geometry dedicated breast CT systems. The cone-beam geometry was based on a configuration studied in the literature.[7] The specifications of the IGCT system were determined by inverting the in-plane cone-beam geometry as illustrated in Fig. **3**. The source-to-detector distance (SDD) was equivalent for both cone-beam and inverse geometries; however, the source-to-isocenter distance (SID) and the detector-to-isocenter distance (DID) were inverted in the inverse geometry. The dimensions of IGCT source and detector in the slice direction were chosen to provide the same longitudinal FOV as the cone-beam system. The inverse-geometry source and detector sampling were based on available hardware components (NovaRay, Inc., Newark, CA). To maintain similar resolution properties, both systems used the same focal spot and detector aperture sizes. The focal spot and aperture sizes are expected to have a negligible effect on the SPR and large-signal CNR.

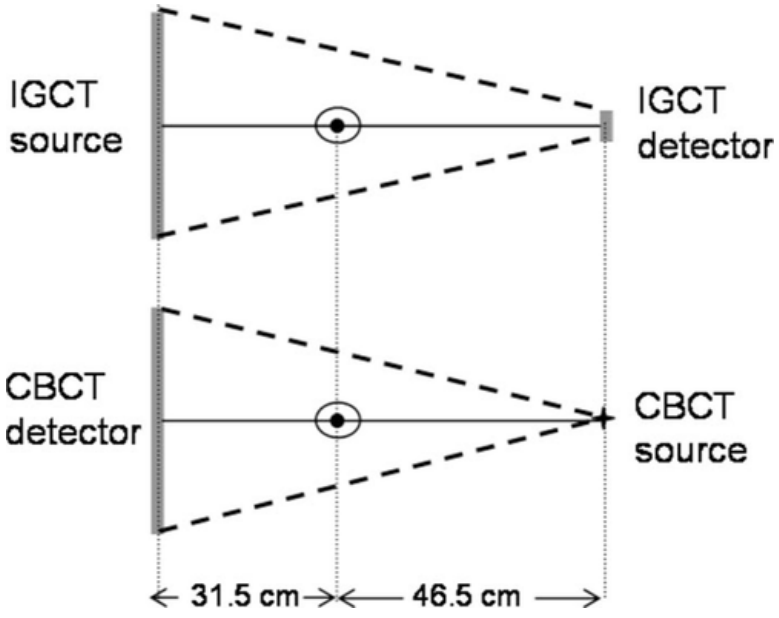

Figure 3 Illustrations of the in-plane (transverse) geometries of the inverse and cone-beam systems. If the IGCT source and cone-beam detector have the same in-plane extent, the coverage is nearly identical when the SID and DID are inverted in the two systems.

Table I. Specifications of simulated IGCT and cone-beam systems.

	IGCT	**Cone beam**
Source dimensions (in plane × slice)	40×18 cm^2	N/A
Number of source positions	160×72	N/A
Detector dimensions (in plane × slice)	54×18 cm^2	40×30 cm^2
Number of detector elements	48×160	1024×768

Focal spot (Gaussian, standard deviation)	$0.183\ \mathrm{mm}$	$0.183\ \mathrm{mm}$
Detector aperture	$1.14\ \mathrm{mm}$	$1.14\ \mathrm{mm}$
Source-to-isocenter distance (SID)	$31.5\ \mathrm{cm}$	$46.5\ \mathrm{cm}$
Source-to-dectector distance (SDD)	$78\ \mathrm{cm}$	$78\ \mathrm{cm}$
FOV (in plane $\times$ slice)	$22 \times 18\ \mathrm{cm}^2$	$22 \times 18\ \mathrm{cm}^2$

Because the mean scatter signal is low frequency and in order to improve the statistics of the Monte Carlo simulations, the IGCT source and cone-beam detector arrays were subsampled in the Monte Carlo simulations by factors of 4 and 2, respectively, from the values listed in Table **I**.

Monte Carlo simulations were performed with the GEANT 4 software library.[39] The simulation software was validated against previously published cone-beam studies.[33] A 164 node high-performance computing cluster provided parallel processing of the Monte Carlo simulations. Monoenergetic simulations were performed at $50\ \mathrm{keV}$ and both systems were simulated with an ideal photon-counting detector. These simplifications facilitate isolating the effects of scatter from the effects of beam hardening and detector efficiency. To verify that the monoenergetic assumption is reasonable for quantifying the relative scatter performance of the inverse and cone-beam geometries, we also performed Monte Carlo simulations with a modeled $80\ \mathrm{kVp}$ spectrum filtered with $3\ \mathrm{mm}$ of aluminum.[40]

The breast phantoms were modeled as cylinders composed of a homogeneous mixture of 50% glandular and 50% adipose tissue. In other words, the phantom was composed of a single material whose elemental composition was the mean of the known compositions of glandular and adipose tissue.[41] Simulations were performed with 10, 14, and $18\ \mathrm{cm}$ diameter phantoms representing a small, an average, and a large breast. The phantom length was equal to 1.5 times the radius.

Because the phantoms are rotationally symmetric, a projection at one view angle was simulated for both the IGCT and cone-beam systems. In the Monte Carlo simulations, all photons are classified as primary when they begin their trajectory from the source to the detector. As the photon trajectory is tracked through the object, the photon is classified as scatter if the interaction at a particular step is Rayleigh or Compton scatter. Fifteen billion x-ray photons were tracked in the cone-beam simulations, as this number was found empirically to result in a 1% standard deviation in the mean scatter signal. One IGCT projection, which is composed of rays connecting every source location to every detector pixel, inherently samples data at a range of azimuthal angles. Therefore, more photons are required for the IGCT simulations and we chose 50×10^9 as a reasonable compromise between runtime and SPR accuracy.

II.B. Scatter-to-primary ratio (SPR)

The SPR of the cone-beam and IGCT projections was calculated by dividing the number of scattered photons reaching each detector pixel by the number of primary photons reaching the pixel. Direct comparison of the cone-beam and IGCT SPR is challenging because one IGCT projection contains many truncated images, one for each source position. In the IGCT acquisition, each source location irradiates the object with a small cone beam; however, if we consider the rays connecting all the source locations to one detector element, the result is a reverse cone-beam image, as shown in Fig. **4**. We rearranged the IGCT data to display rays connecting all source locations to the central pixel in the top detector row. The SPR of this IGCT reverse projection was compared to the conventional cone-beam projection. In order to compare the overall SPR, we plotted histograms of SPR for all rays that pass through the phantoms in both geometries.

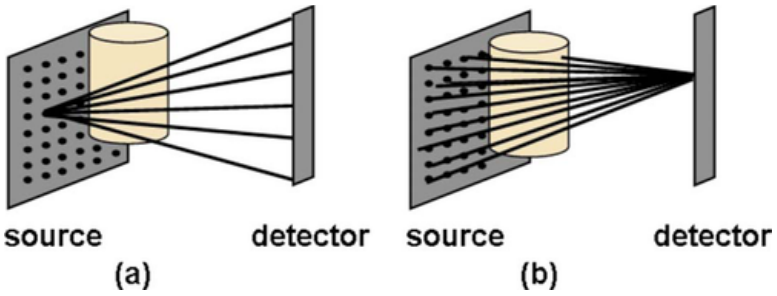

Figure 4 (a) The IGCT data as they are acquired. At each source location a small cone beam is emitted and collimated towards the detector. (b) An IGCT reverse cone-beam projection consisting of rays that connect one detector pixel to all source locations.

In the inverted geometry, the increased air gap and the rapid fractional scanning of the object both act to reduce scatter. To understand the contribution of air gap, the cone-beam Monte Carlo simulation was modified to have the same DID as the IGCT system (DID increased from 31.5 to 46.5 cm) and the resulting SPR profiles compared. If the SID is held constant, the detector area must increase with the air gap in order to maintain the field of view.

II.C. Contrast-to-noise ratio (CNR)

In addition to quantifying the amount of scattered radiation, it is important to quantify the effects of scatter on the reconstructed image. We investigated the effects of scatter on the CNR in reconstructed images of tumors in breast tissue. To isolate the effects of scatter from those of beam hardening, all simulations assumed a monoenergetic 50 keV beam.

II.C.1. Simulation procedure

We simulated cone-beam and inverse-geometry systems with specifications listed in Table **I**. Five hundred view angles were simulated for the cone-beam system. For the IGCT simulations, projections at 55 view angles were simulated as this number was found to provide sufficient sampling (the IGCT system requires fewer views because each view samples a range of azimuthal angles).[35] The breast phantoms in this study were cylinders composed of 50% glandular/50% adipose tissue containing four spherical invasive ductal carcinoma (IDC) tumors of diameters of 2, 1, 0.75, and 0.5 cm. All tumors were centered 1.5 cm from the top of the breast and 3.5 cm from the center of rotation.

While the SPR can be quantified in one projection, projections at 360° must be simulated in order to reconstruct images. Reduction in simulation time is possible if we assume that the mean scatter signal is constant across view angles. While this assumption is true for the cylinder breast phantoms, the addition of the off-centered tumors removes the rotational symmetry of the phantoms. However, the tumors are small, low-contrast objects and are unlikely to considerably alter the scatter signal. To validate this assumption, we performed a Monte Carlo simulation of the 18 cm diameter cylinder with and without a 2 cm diameter tumor located at the isocenter and compared the resulting scatter projections. Once the assumption was validated, the scatter projections simulated in the SPR study were used to calculate the mean scatter signal for all view angles.

The Monte Carlo simulations used in this study model the stochastic transport of photons but not the stochastic generation of photons. The process of photon generation is responsible for the Poisson distribution of x-ray measurements.[42] To generate projections with proper noise statistics, we simulated cone-beam and inverse-geometry projections in three steps: (1) analytically simulated fully sampled primary projections and (2) mean scatter projections obtained from Monte Carlo simulations and (3) addition of noise representative of a realistic breast CT scan. The simulation procedure is described in more detail below.

For both the IGCT and cone-beam systems, the line integral through the phantom was calculated analytically assuming the known attenuation coefficient of breast tissues.[43] The mean scatter projection S was estimated by denoising the Monte Carlo scatter projections with the Richardson–Lucy fitting algorithm followed by bilinear interpolation to match the fully sampled analytical projections. The Richardson–Lucy algorithm was previously proposed for denoising scatter projections obtained through Monte Carlo simulation.[44] The mean detected signal for a detector pixel, $\bar{P}(i,j)$, that measures photons along ray path s is

$$\bar{P}(i,j) = N \cdot \left(\exp\left[- \int \mu(x,y,z) ds \right] + \frac{S(i,j)}{N_{\mathrm{MC}}} \right),$$

(1)

where N is the number of simulated incident photons per ray and N_{MC} is the number of incident photons per ray in the Monte Carlo simulation. The noise in an x-ray measurement is Poisson distributed with mean and variance equal to the total number of detected counts (primary and scatter).[42] We first verified that the detected photon flux was sufficiently large to approximate Poisson noise with additive Gaussian noise and then simulated noisy projection data as

$$\tilde{P}(i,j) = \bar{P}(i,j) + n(0, \bar{P}(i,j)),$$

(2)

where $n(m, \sigma^2)$ is Gaussian noise with mean m and variance σ^2. In order to generate images with realistic standard deviation, a realistic number of photons, N, must be simulated. Boone *et al.* determined the photon fluence at the isocenter of a breast CT system which imparts radiation dose equivalent to a two-view mammogram for different breast diameters.[4] The photon fluence was found to be nearly independent of kVp. To estimate the total number of photons (Table II) required in our simulations to represent a realistic breast CT scan, we multiplied the published photon fluence values at 80 kVp by the area of the beam at the isocenter for the cone-beam geometry specified in Table I. For each of the cone-beam and inverse geometries, the number of photons per ray, N, was calculated by dividing the values in Table II by the number of rays per view and the number of view angles. We simulated photon fluence representing dose equivalent to two-view mammography for each breast diameter; however, this dose level varies with breast size.[4]

Table II. Number of simulated photons per acquisition

Breast diameter	Number of photons
10 cm	1.6×10^{12}
14 cm	7.8×10^{12}
18 cm	1.9×10^{13}

Finally, the projection data, $\tilde{P}$, were normalized by the number of incident photons, N, and the logarithm performed prior to reconstruction. Cone-beam data were reconstructed with the Feldkamp algorithm, and IGCT data were reconstructed with the FORE-J algorithm.[45–47] Figure **5** summarizes the simulation and reconstruction procedure. The simulations were repeated five times for each of the cone-beam and IGCT geometries and for each of the three breast diameters.

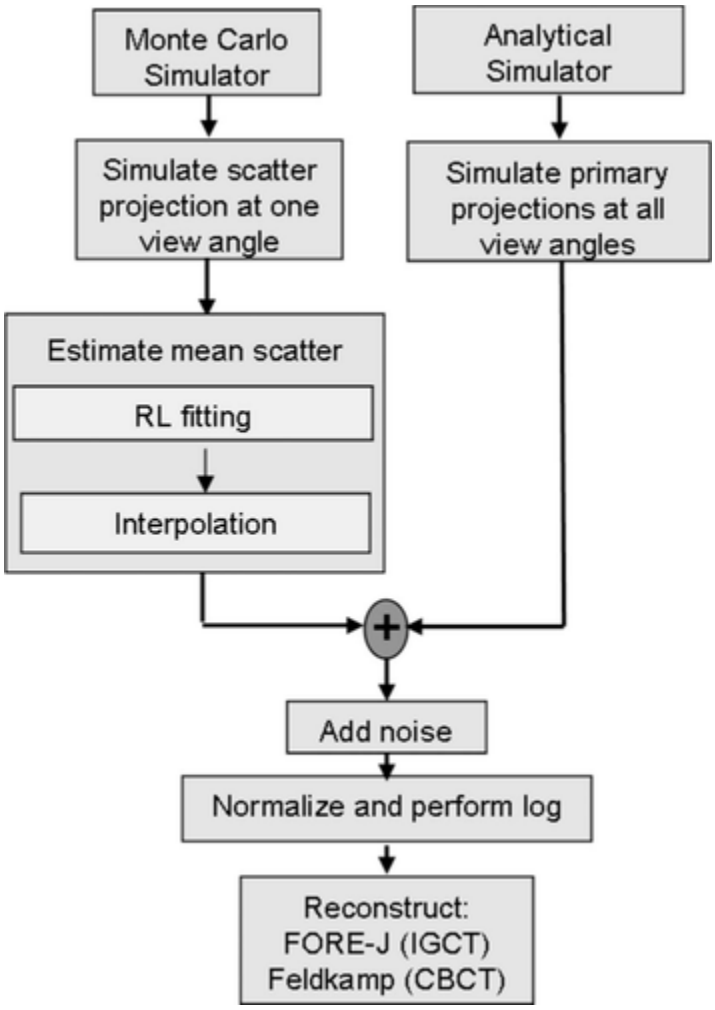

Figure 5 A flow chart detailing the steps for simulating and reconstructing IGCT and cone-beam images.

It is important to simulate cone-beam and IGCT systems with equivalent spatial resolution and dose, so that any differences in CNR are due to scatter. To approximate comparable dose, we simulated both systems with the same total number of photons, representing the photon fluence at the isocenter of a breast CT scan with dose equivalent to mammography. To approximate equivalent spatial resolution, the backprojection filter in both reconstruction algorithms was apodized with a Hanning window with a cutoff of $8\ \mathrm{lp/cm}$. To verify that both systems have the same spatial resolution, the modulation transfer function (MTF) was calculated by simulating a $100\ \mu\mathrm{m}$ diameter sphere centered at the isocenter on the plane $1.5\ \mathrm{cm}$ from the top of the breast.

II.C.2. CNR measurement

For all simulations, the central axial slice through the tumors was reconstructed with pixels of 0.25 by $0.25\ \mathrm{mm}$. Two 40 by 40 pixel regions of interest (ROIs) equidistant from the isocenter were extracted from the reconstructed images: one ROI contained only tumor and the other only breast background. The mean (HU) and standard deviation (σ) of the CT numbers were determined in each ROI, and the CNR between tumor and breast background was calculated with Eq. (3). The mean and standard deviation of the CNR over the five trials were also calculated,

$$\mathrm{CNR} = \frac{\mathrm{HU}_{\mathrm{tumor}} - \mathrm{HU}_{\mathrm{background}}}{\sigma_{\mathrm{background}}}. \quad (3)$$

The relationship between SPR and CNR is described analytically in Eq. (4) where CNR_o is the nominal CNR in the absence of scatter.[24] Based on this relationship, the CNR improvement factor of the IGCT compared to cone beam, F_{CNR}, can be calculated [Eq. (5)],

$$\mathrm{CNR}_{\mathrm{scatter}} = \mathrm{CNR}_o \cdot \frac{1}{\sqrt{1+\mathrm{SPR}}}, \tag{4}$$

$$F_{\mathrm{CNR}} = \frac{\mathrm{CNR}_{\mathrm{IGCT}}}{\mathrm{CNR}_{\mathrm{CBCT}}} = \sqrt{\frac{1+\mathrm{SPR}_{\mathrm{CBCT}}}{1+\mathrm{SPR}_{\mathrm{IGCT}}}}. \tag{5}$$

II.C.3. Scatter correction

Some form of scatter correction will likely be performed in cone-beam breast CT to reduce the effects of scatter; therefore we also compared the IGCT images to scatter-corrected cone-beam images. The scatter-corrected projection, $\tilde{P}_{\mathrm{corrected}}$, was obtained by subtracting the mean scatter signal from the noisy projection data prior to reconstruction, as described in Eq. (6). This correction scheme eliminates the deterministic effects of scatter and represents an ideal correction that would be difficult to achieve in practice, where the mean scatter signal must be estimated through postprocessing or experimental measurement,

$$\tilde{P}_{\mathrm{corrected}}(i,j) = \tilde{P}(i,j) - S(i,j). \tag{6}$$

III. RESULTS

III.A. Scatter-to-primary ratio (SPR)

Figure **6** plots the SPR of cone-beam projections and IGCT reverse cone-beam projections of the three breast phantoms at 50 keV (solid lines) and 80 kVp (dotted lines). Published experimental SPR results, measured at 80 kVp, are also plotted.[7] All profiles represent projections at a 4° cone angle. Table **III** summarizes the peak SPR averaged over the central 1 cm of the detector. The monoenergetic and polyenergetic simulations resulted in similar SPR curves; therefore all subsequent simulations assume a monoenergetic 50 keV beam.

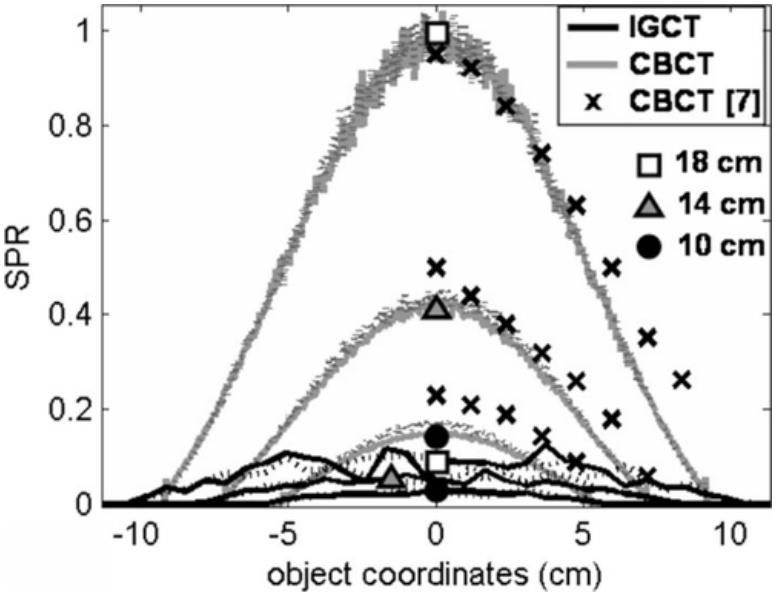

Figure 6 SPR profiles of simulated cone-beam projections and IGCT reverse projections for the three breast diameters. The solid lines represent the monoenergetic 50 keV simulations, while the dotted lines represent the polyenergetic 80 kVp simulations. Published experimental cone-beam results are also plotted (Ref. **7**).

Table III. Peak SPR for three breast diameters.

	10 cm	**14 cm**	**18 cm**
IGCT (50 keV)	0.03	0.05	0.09
IGCT (80 kVp)	0.02	0.06	0.09
CBCT (50 keV)	0.15	0.42	0.99
CBCT (80 kVp)	0.18	0.44	0.98

The profiles plotted in Fig. **6** represent a subset of the projection data. To further compare the SPR of the two geometries, Fig. **7** displays histograms of SPR for all rays that pass through the phantoms.

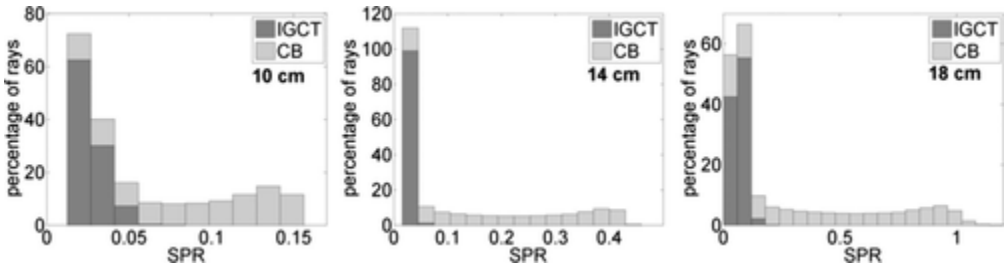

Figure 7 Histograms comparing the SPR of IGCT and cone-beam rays that pass through the 10, 14, and 18 cm diameter breast phantoms.

Figure **8** compares the SPR of a cone-beam system with DIDs of 31.5 and 46.5 cm. The increase in air gap reduces the SPR from 0.41 to 0.31 for the cone-beam system compared to a SPR of 0.05 for the IGCT system with 46.5 cm DID.

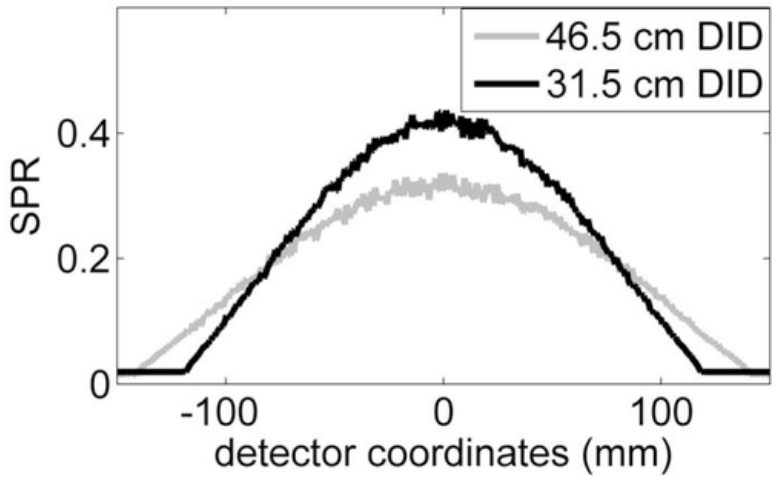

Figure 8 SPR profiles of a cone-beam system with the originally specified DID $(31.5$ cm$)$ and with DID matched to the IGCT system $(46.5$ cm$)$. The object is the 14 cm diameter phantom.

Overall, the SPR is an order of magnitude lower for the IGCT system compared to the cone-beam system. The simulated results are in reasonable agreement with the published experimental SPR measurements.

III.B. Contrast-to-noise ratio (CNR)

In our methods we assumed that the low-contrast tumors do not affect the scatter projection. Figure **9** supports this assumption, plotting the scatter projection of an $18\ \mathrm{cm}$ diameter breast phantom with and without a $2\ \mathrm{cm}$ diameter tumor. The displayed profile corresponds to the projection through the center of the tumor. Based on this result, the mean scatter projection simulated at one view angle was used to generate projections at all views. A second assumption in our methods was that both the cone-beam and IGCT systems have comparable spatial resolution. Figure **10** plots the in-plane MTF of the two systems, demonstrating that both systems are operating with similar spatial resolution. A third assumption was that the Poisson photon noise could be simulated with additive Gaussian noise. The minimum number of expected detected counts across all pixels in all simulations was 37 counts, with most pixels detecting several hundred or thousand counts. The Gaussian approximation is reasonable based on this number of expected counts.

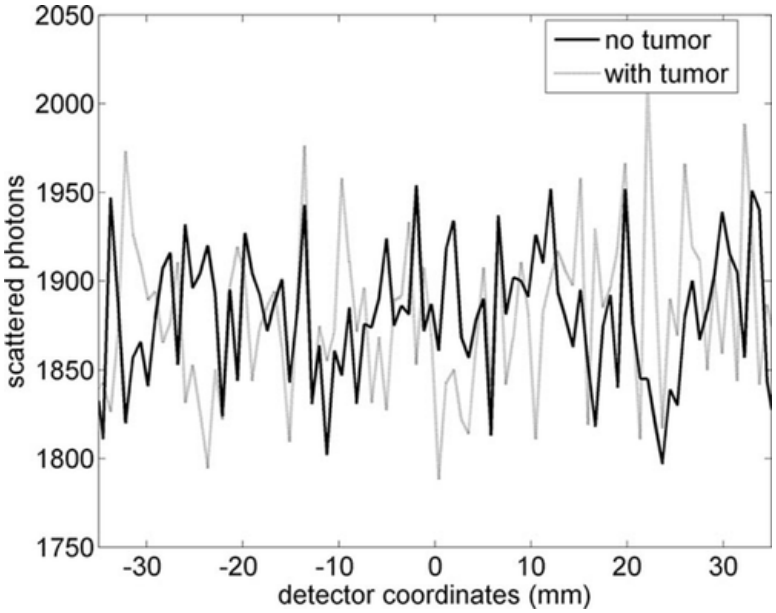

Figure 9 Detected scatter for an $18\ \mathrm{cm}$ diameter breast phantom with and without a $2\ \mathrm{cm}$ diameter tumor at the isocenter.

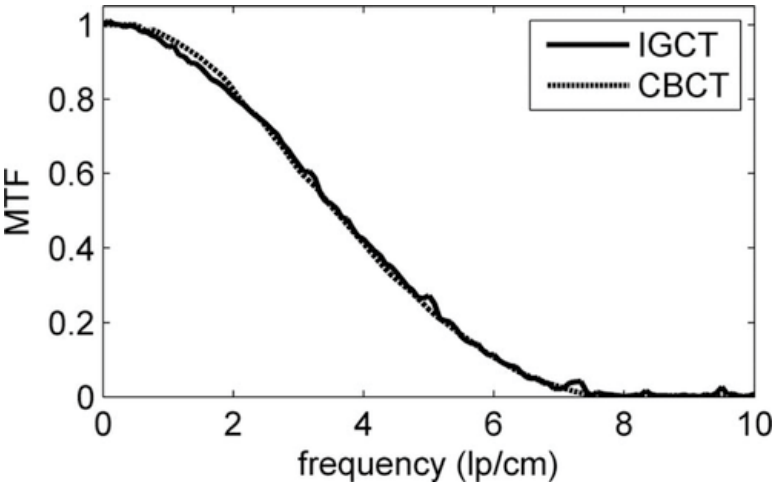

Figure 10 MTF of the simulated IGCT and cone-beam systems. The MTF is considerably worse than that reported in Ref. **36** because of the different SDDs and DIDs and because the MTF in this case is limited by the $8\ \mathrm{lp/cm}$ bandwidth of the reconstruction filter.

Figure **11** compares the reconstructed cone-beam and IGCT images of the $18\ \mathrm{cm}$ diameter breast in the absence of scatter. All images are windowed to display values between -500 and $200\ \mathrm{HU}$. Images of the $18\ \mathrm{cm}$ phantom including the effects of scatter are shown in Fig. **12**. IGCT images are compared to cone-beam images with and without ideal scatter correction.

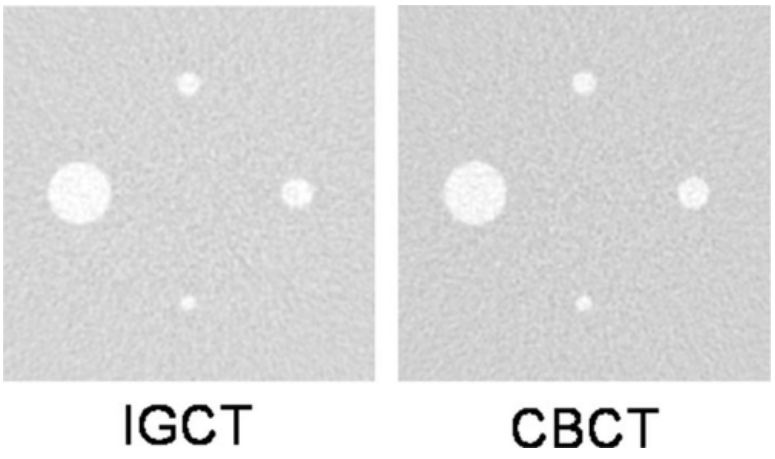

Figure 11 Reconstructed axial images of the $18\ \mathrm{cm}$ diameter breast phantom simulated without the effects of scatter. The phantom contains IDC tumors of 0.5, 0.75, 1, and $2\ \mathrm{mm}$ diameters. All images are windowed to display CT numbers from -500 to $200\ \mathrm{HU}$.

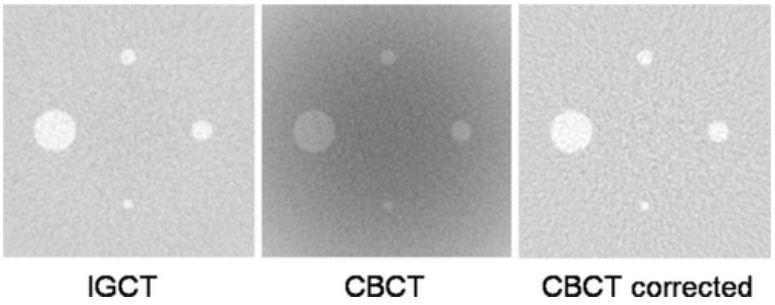

Figure 12 Reconstructed axial images of the $18\ \mathrm{cm}$ diameter breast phantoms simulated with scatter. The cone-beam system was reconstructed with and without ideal scatter correction. All images are windowed from -500 to $200\ \mathrm{HU}$.

To better visualize the effects of scatter, Fig. **13** plots the central horizontal profiles of the reconstructed images. The cupping artifacts seen in the cone-beam images are absent in the IGCT images. As expected, the ideal cone-beam scatter correction eliminates the cupping artifact and recovers the contrast; however, the stochastic scatter signal remains and thus the noise is increased.

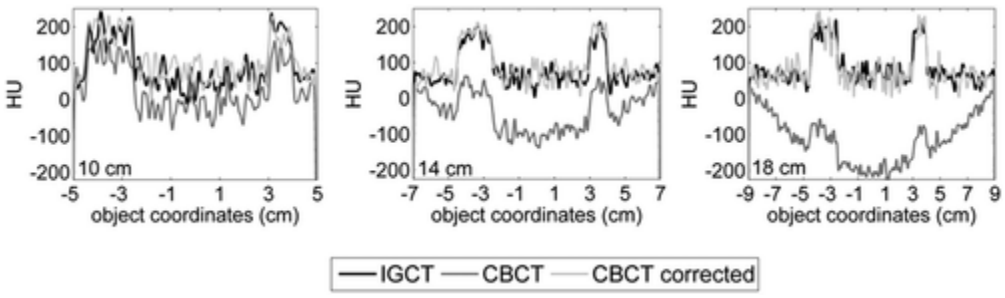

Figure 13 Central horizontal profiles through axial breast phantom images.

The CNR of the IGCT and cone-beam images are plotted in Figs. **14 and 15**, with error bars depicting the standard deviation of the CNR measurement across the five simulation trials.

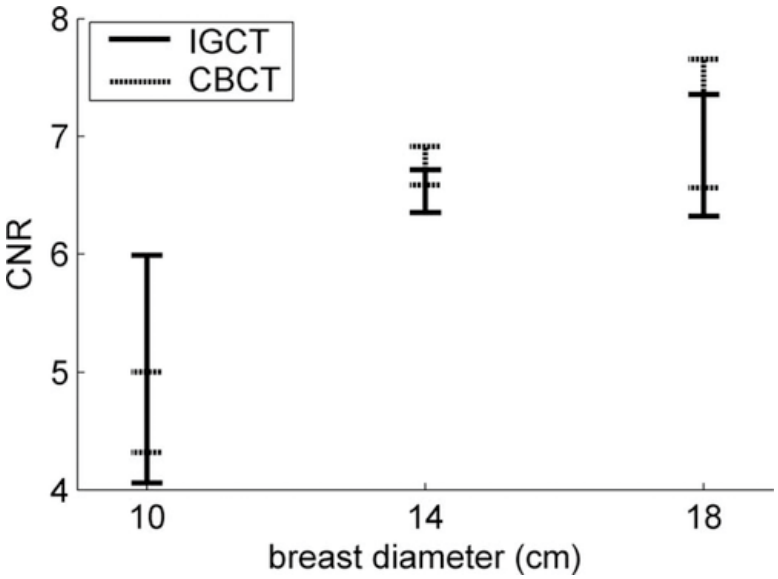

Figure 14 CNR in the absence of scatter. The error bars represent the standard deviation across five trials.

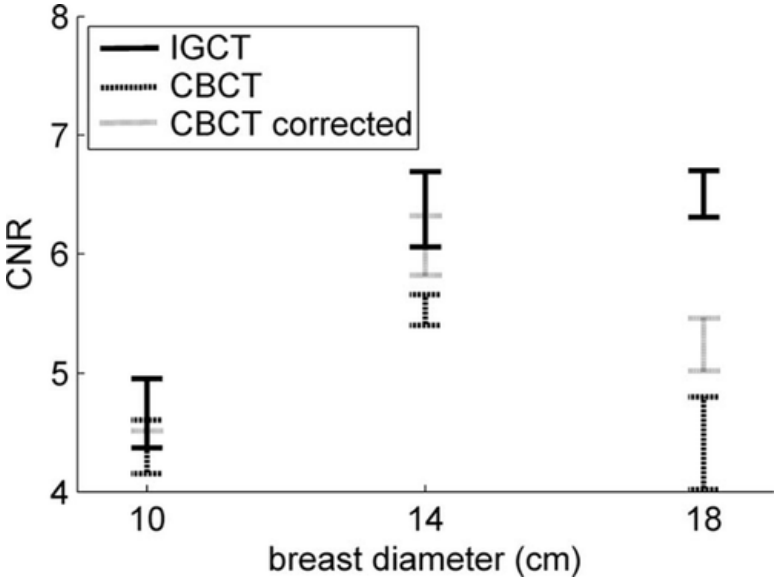

Figure 15 CNR of images simulated with scatter. The error bars represent the standard deviation across five trials.

The results demonstrate that in the absence of scatter, the IGCT and cone-beam images have comparable CNR. When the effects of scatter are included, the inverse geometry improves the CNR compared to an uncorrected cone-beam acquisition by a factor of 1.16 for the 14 cm diameter breast and 1.48 for the 18 cm diameter breast. Analytical predictions based on the SPR results [Eq. **(4)**] estimate CNR improvement factors of 1.16 and 1.35 for the 14 and 18 cm phantoms. The difference in CNR is negligible for the 10 cm breast. Compared to a cone-beam reconstruction with an ideal scatter correction, the IGCT system has a factor of 1.25 improvement in CNR for the 18 cm diameter breast and a negligible improvement for the smaller phantoms.

IV. DISCUSSION AND CONCLUSIONS

The results indicate that the inverse geometry reduces the SPR by an order of magnitude and that the majority of the scatter reduction is due to the fractional scanning of the IGCT system. For example, when comparing systems with equivalent but inverted in-plane geometries, the SPR was reduced by 88% for the $14\ \mathrm{cm}$ diameter breast. When comparing systems with equivalent air gap, the inverse geometry reduced the scatter by 84%. As demonstrated in Fig. **6** and Table **III**, the SPR increases more rapidly with breast dimensions for the cone-beam system compared to the IGCT system. In our simulations, the length of the breast phantoms increased linearly with the diameter. In the cone-beam geometry, the size of the beam needed to irradiate the object increases in both the in-plane and slice directions with increased breast dimensions. In the IGCT system, the size of the beam in the in-plane directions is fixed by the $5.4\ \mathrm{cm}$ detector extent; therefore the scatter increases only with breast length.

The presented study was designed to quantify the effects of the inverse geometry on scatter as independently of specific hardware components as possible. Therefore, both inverse-geometry and cone-beam systems were simulated with ideal photon-counting detectors. Energy-integrating detectors weigh each incoming photon by its energy, thereby giving less weight to the low energy photons. Photon-counting detectors weigh all photons equally. Because the detected scatter spectrum is softer than the primary spectrum, photon counting will amplify the scatter signal compared to energy integrating. On the other hand, by increasing the threshold above which photons are counted, photon-counting detectors can reject some scattered photons. Quantifying the scatter effects of photon counting versus energy integrating is important for all CT geometries and requires further study.

The ideal scatter correction implemented in this study relies on knowledge of the true mean scatter signal, a scenario that is difficult to achieve in practice. Methods that correct the cupping artifact do not necessarily recover the loss in contrast due to scatter, as is the case for the scatter correction algorithm specifically proposed for breast CT.[34] Overall, we expect the IGCT images to have a non-negligible improvement in CNR compared to cone-beam images reconstructed with realizable scatter correction methods for the average $(14\ \mathrm{cm})$ and large $(18\ \mathrm{cm})$breast sizes.

Our results demonstrate a factor of 1.48 improvement in CNR with the inverse geometry for the $18\ \mathrm{cm}$ diameter breast compared to a cone-beam acquisition with no scatter correction or a cupping-only correction. Compared to a cone-beam acquisition with an ideal scatter correction, the IGCT system provided a 1.25 improvement in CNR. Because the noise standard deviation in a CT reconstruction is inversely proportional to the square root of exposure, our results predict that the IGCT system can provide the same CNR as the cone-beam system (without scatter correction) at 46% of the dose for the $18\ \mathrm{cm}$ diameter breast and at 74% of the dose for the $14\ \mathrm{cm}$ breast.[23] Compared to a cone-beam system with an ideal scatter correction, the IGCT system provides the same CNR at 64% of the dose for the $18\ \mathrm{cm}$ breast. Additional dose efficiency is expected in the IGCT system due to the increased detective quantum efficiency of the photon-counting detector.[48]

The clinical feasibility of inverse-geometry breast CT requires further investigation. A prototype breast IGCT system must be developed to experimentally measure the scatter and general performance of the proposed system. Future work must investigate the effects of the photon-counting detector and quantify the performance of inverse-geometry breast CT relative to specific imaging tasks, for example, the detection of masses.

Overall, the inverse geometry provided an order of magnitude reduction in SPR compared to a cone-beam system, leading to CNR improvements of 1.16–1.48 (no cone-beam scatter correction) and 1.03–1.25 (ideal cone-beam scatter correction) for average and large breast phantoms. This improvement in CNR can be leveraged to reduce the dose or to improve the contrast and/or spatial resolution. The improved scatter

performance of the IGCT system may be advantageous for dedicated breast CT scanning, a modality that requires high-contrast resolution, spatial resolution, and dose efficiency.

ACKNOWLEDGMENTS

Computer simulations were performed on the Marquette University High Performance Computing Cluster (NSF Grant No.CTS-0521602). The authors would like to thank Lars E. Olson, Ph.D. (Marquette University), for help with the cluster, Lei Zhu, Ph.D. (Stanford University), for assistance with GEANT4, and Samual R. Mazin, Ph.D. (Stanford University), for providing the FORE-J reconstruction software.

REFERENCES

1 J. M. Boone, T. R. Nelson, K. K. Lindfors, and J. A. Seibert, "Dedicated breast CT: Radiation dose and image quality evaluation," *Radiology* 10.1148/radiol.2213010334 **221**(3), 657– 67 (2001).

2 B. Chen and R. Ning, "Cone-beam volume CT breast imaging: Feasibility study," *Med. Phys.* 10.1118/1.1461843 **29**(5), 755– 70 (2002).

3 J. M. Boone, N. Shah, and T. R. Nelson, "A comprehensive analysis of DgN(CT) coefficients for pendant-geometry cone-beam breast computed tomography," *Med. Phys.* 10.1118/1.1636571 **31**(2), 226– 35 (2004).

4 J. M. Boone, A. L. Kwan, J. A. Seibert, N. Shah, K. K. Lindfors, and T. R. Nelson, "Technique factors and their relationship to radiation dose in pendant geometry breast CT," *Med. Phys.* 10.1118/1.2128126 **32**(12), 3767– 76 (2005).

5 J. M. Boone, A. L. Kwan, K. Yang, G. W. Burkett, K. K. Lindfors, and T. R. Nelson, "Computed tomography for imaging the breast," *J Mammary Gland Biol Neoplasia* **11**(2), 103– 111 (2006).

6 S. J. Glick, S. Thacker, X. Gong, and B. Liu, "Evaluating the impact of x-ray spectral shape on image quality in flat-panel CT breast imaging," *Med. Phys.* 10.1118/1.2388574 **34**(1), 5– 24 (2007).

7 A. L. Kwan, J. M. Boone, and N. Shah, "Evaluation of x-ray scatter properties in a dedicated cone-beam breast CT scanner," *Med. Phys.* 10.1118/1.1954908 **32**(9), 2967– 2975 (2005).

8 X. Gong, A. A. Vedula, and S. J. Glick, "Microcalcification detection using cone-beam CT mammography with a flat-panel imager," *Phys. Med. Biol.* 10.1088/0031-9155/49/11/005 **49**(11), 2183– 95 (2004).

9 X. Gong, S. J. Glick, B. Liu, A. A. Vedula, and S. Thacker, "A computer simulation study comparing lesion detection accuracy with digital mammography, breast tomosynthesis, and cone-beam CT breast imaging," *Med. Phys.* 10.1118/1.2174127 **33**(4), 1041– 1052 (2006).

10 S. C. Thacker and S. J. Glick, "Normalized glandular dose (DgN) coefficients for flat-panel CT breast imaging," *Phys. Med. Biol.* 10.1088/0031-9155/49/24/003 **49**(24), 5433– 5444 (2004).

11 R. L. McKinley, M. P. Tornai, E. Samei, and M. L. Bradshaw, "Simulation study of a quasi-monochromatic beam for x-ray computed mammotomography," *Med. Phys.* 10.1118/1.1668371 **31**(4), 800– 813 (2004).

12 C. J. Lai, C. C. Shaw, L. Chen, M. C. Altunbas, X. Liu, T. Han, T. Wang, W. T. Yang, G. J. Whitman, and S. J. Tu, "Visibility of microcalcification in cone beam breast CT: effects of x-ray tube voltage and radiation dose," *Med. Phys.* 10.1118/1.2745921 **34**(7), 2995– 3004 (2007).

13 K. Yang, A. L. Kwan, and J. M. Boone, "Computer modeling of the spatial resolution properties of a dedicated breast CT system," *Med. Phys.* 10.1118/1.2737263 **34**(6), 2059– 2069 (2007).

14 I. Sechopoulos, S. Vedantham, S. Suryanarayanan, C. J. D'Orsi, and A. Karellas, "Monte carlo and phantom study of the radiation dose to the body from dedicated CT of the breast," *Radiology* **247**(1), 98– 105 (2008).

15 W. T. Yang, S. Carkaci, L. Chen, C. J. Lai, A. Sahin, G. J. Whitman, and C. C. Shaw, "Dedicated cone-beam breast CT: feasibility study with surgical mastectomy specimens," *AJR, Am. J. Roentgenol.* 10.2214/AJR.07.2403 **189**(6), 1312– 1315 (2007).

16 K. K. Lindfors, J. M. Boone, T. R. Nelson, K. Yang, A. L. Kwan, and D. F. Miller, "Dedicated breast CT: Initial clinical experience," *Radiology* 10.1148/radiol.2463070410 **246**(3), 725– 733 (2008).

17 B. D. Smith, " Cone-beam tomography: Recent advances and a tutorial review," *Opt. Eng.* 10.1117/1.2168899 **29**(5), 524– 534 (1990).
18 R. Ning, X. Tang, D. Conover, and R. Yu, "Flat panel detector-based cone beam computed tomography with a circle-plus-two-arcs data acquisition orbit: preliminary phantom study," *Med. Phys.* 10.1118/1.1582470 **30**(7), 1694– 1705 (2003).
19 X. Tang and R. Ning, "A cone beam filtered backprojection (CB-FBP) reconstruction algorithm for a circle-plus-two-arc orbit," *Med. Phys.* 10.1118/1.1376444 **28**(6), 1042– 1055 (2001).
20 K. Zeng, H. Yu, L. L. Fajardo, and G. Wang, "Cone-beam mammo-computed tomography from data along two tilting arcs," *Med. Phys.* 10.1118/1.2336510 **33**(10), 3621– 3633 (2006).
21 P. M. Joseph and R. D. Spital, "The effects of scatter in x-ray computed tomography," *Med. Phys.* 10.1118/1.595111 **9**(4), 464– 472 (1982).
22 G. H. Glover, "Compton scatter effects in CT reconstructions," *Med. Phys.* 10.1118/1.595197 **9**(6), 860– 867 (1982).
23 J. H. Siewerdsen and D. A. Jaffray, "Cone-beam computed tomography with a flat-panel imager: Magnitude and effects of x-ray scatter," *Med. Phys.* 10.1118/1.1339879 **28**(2), 220– 231 (2001).
24 M. Endo, S. Mori, T. Tsunoo, and H. Miyazaki, "Magnitude and effects of x-ray scatter in a 256-slice CT scanner," *Med. Phys.* 10.1118/1.2239366 **33**(9), 3359– 3368 (2006).
25 J. H. Siewerdsen, D. J. Moseley, B. Bakhtiar, S. Richard, and D. A. Jaffray, "The influence of antiscatter grids on soft-tissue detectability in cone-beam computed tomography with flat-panel detectors," *Med. Phys.* 10.1118/1.1819789 **31**(12), 3506– 3520 (2004).
26 P. M. Shikhaliev, T. Xu, and S. Molloi, "Photon counting computed tomography: Concept and initial results," *Med. Phys.* 10.1118/1.1854779 **32**(2), 427– 436 (2005).
27 J. A. Sorenson and J. Floch, "Scatter rejection by air gaps: An empirical model," *Med. Phys.* 10.1118/1.595690 **12**(3), 308– 316 (1985).
28 J. A. Seibert and J. M. Boone, "X-ray scatter removal by deconvolution," *Med. Phys.* 10.1118/1.596208 **15**(4), 567– 575 (1988).
29 Y. Kyriakou, T. Riedel, and W. A. Kalender, "Combining deterministic and Monte Carlo calculations for fast estimation of scatter intensities in CT," *Phys. Med. Biol.* 10.1088/0031-9155/51/18/008 **51**(18), 4567– 4586 (2006).
30 R. Ning, X. Tang, and D. Conover, "X-ray scatter correction algorithm for cone beam CT imaging," *Med. Phys.* 10.1118/1.1711475 **31**(5), 1195– 202 (2004).
31 W. Zbijewski and F. J. Beekman, "Efficient Monte Carlo based scatter artifact reduction in cone-beam micro-CT," *IEEE Trans. Med. Imaging* 10.1109/TMI.2006.872328 **25**, 817– 827 (2006).
32 M. Honda, K. Kikuchi, and K. Komatsu, "Method for estimating the intensity of scattered radiation using a scatter generation model," *Med. Phys.* 10.1118/1.596710 **18**(2), 219– 226 (1991).
33 L. Zhu, N. R. Bennett, and R. Fahrig, "Scatter correction method for x-ray CT using primary modulation: Theory and preliminary results," *IEEE Trans. Med. Imaging* 10.1109/TMI.2006.884636 **25**, 1573– 1587 (2006).
34 M. C. Altunbas, C. C. Shaw, L. Chen, C. Lai, X. Liu, T. Han, and T. Wang, "A post-reconstruction method to correct cupping artifacts in cone beam breast computed tomography," *Med. Phys.* 10.1118/1.2748106 **34**(7), 3109– 3118 (2007).
35 T. G. Schmidt, R. Fahrig, N. J. Pelc, and E. G. Solomon, "An inverse-geometry volumetric CT system with a large-area scanned source: A feasibility study," *Med. Phys.* 10.1118/1.1786171 **31**(9), 2623– 2627 (2004).
36 T. G. Schmidt, J. Star-Lack, N. R. Bennett, S. R. Mazin, E. G. Solomon, R. Fahrig, and N. J. Pelc, "A prototype table-top inverse-geometry volumetric CT system," *Med. Phys.* 10.1118/1.2192887 **33**(6), 1867– 1878 (2006).
37 E. G. Solomon, B. P. Wilfley, M. S. Van Lysel, A. W. Joseph, and J. A. Heanue, "Scanning-beam digital x-ray (SBDX) system for cardiac angiography," *Medical Imaging 1999: Physics of Medical Imaging* (SPIE, San Diego, CA, 1999), Vol. **3659**, pp. 246– 257.

38 J. A. Heanue, D. A. Pearson, and R. E. Melen, "CdZnTe detector array for a scanning-beam digital x-ray system," *Medical Imaging 1999: Physics of Medical Imaging* (SPIE, San Diego, CA, 1999), Vol. **3659**, pp. 718– 725.
39 S. Agostinelli *et al.*, "G4-a simulation toolkit," *Nucl. Instrum. Methods Phys. Res. A* 10.1016/S0168-9002(03)01368-8 **506**(3), 250– 303 (2003).
40 J. M. Boone and J. A. Seibert, "An accurate method for computer-generating tungsten anode x-ray spectra from 30 to 140 kv," *Med. Phys.* 10.1118/1.597953 **24**(11), 1661– 1670 (1997).
41 G. R. Hammerstein, D. W. Miller, D. R. White, M. E. Masterson, H. Q. Woodard, and J. S. Laughlin, "Absorbed radiation dose in mammography," *Radiology* **130**(2), 485– 491 (1979).
42 A. Macovski, *Medical Imaging Systems* (Prentice-Hall, Upper Saddle River, NJ, 1983).
43 P. C. Johns and M. J. Yaffe, "X-ray characterisation of normal and neoplastic breast tissues," *Phys. Med. Biol.* 10.1088/0031-9155/32/6/002 **32**(6), 675– 695 (1987).
44 A. P. Colijn and F. J. Beekman, "Accelerated simulation of cone beam x-ray scatter projections," *IEEE Trans. Med. Imaging* 10.1109/TMI.2004.825600 **23**(5), 584– 590 (2004).
45 L. A. Feldkamp, L. C. Davis, and J. W. Kress, "Practical cone-beam algorithm," *J. Opt. Soc. Am. A* 10.1364/JOSAA.1.000612 **1**(6), 612– 619 (1984).
46 M. Defrise and X. Liu, "A fast rebinning algorithm for 3D positron emission tomography using John's equation," *Inverse Probl.* 10.1088/0266-5611/15/4/314 **15**, 1047– 1065 (1999).
47 S. R. Mazin and N. J. Pelc, "A fast 3D reconstruction algorithm for inverse-geometry CT based on an exact pet rebinning algorithm," *Medical Imaging 2007: Physics of Medical Imaging* (SPIE, San Diego, CA, 2007), Vol. **6510**, p. 65105C– 8.
48 M. J. Tapiovaara and R. Wagner, "Snr and dqe analysis of broad spectrum x-ray imaging," *Phys. Med. Biol.* 10.1088/0031-9155/30/6/002 **30**(6), 519– 529 (1985).